

1 **Effects of three-dimensional electric field on saltation**  
2 **during dust storms: An observational and numerical**  
3 **study**

4

5 Huan Zhang<sup>1</sup>, You-He Zhou<sup>1,\*</sup>

6

7 <sup>1</sup>Department of Mechanics and Engineering Science, College of Civil Engineering and  
8 Mechanics, Lanzhou University, Key Laboratory of Mechanics on Disaster and  
9 Environment in Western China, The Ministry of Education of China, Lanzhou 730000,  
10 PR China.

11

12 \*Correspondence to: You-He Zhou ([zhouyh@lzu.edu.cn](mailto:zhouyh@lzu.edu.cn))

13

1 **Abstract.** Particle triboelectric charging being ubiquitous in nature and industry,  
2 potentially plays a key role in dust events, including the lifting and transport of sand  
3 and dust particles. However, the properties of the electric field (E-field) and its  
4 influences on saltation during dust storms remain obscure as the high complexity of  
5 dust storms and the existing numerical studies mainly limited to one-dimensional (1-  
6 D) E-field. Here, we quantify the effects of real three-dimensional (3-D) E-field on  
7 saltation, through a combination of field observations and numerical modelling. The  
8 3-D E-fields in the sub-meter layer from 0.05 to 0.7 m above the ground during a dust  
9 storm are measured at Qingtu Lake Observation Array site. [The time-varying mean of](#)  
10 [E-field series over the timescales of about 17 minutes are extracted by the discrete](#)  
11 [wavelet transform \(DWT\) and ensemble empirical mode decomposition \(EEMD\)](#)  
12 [methods.](#) The measured results show that each component of the 3-D E-field data  
13 [roughly](#) collapses on a single 3-order polynomial curve when normalized. Such 3-D E-  
14 field data close to the ground within a few centimeters has never been reported and  
15 formulated before. Using the discrete element method, we then develop a  
16 comprehensive saltation model, in which the triboelectric charging between particle-  
17 particle midair collisions is explicitly accounted for, allowing us to evaluate the  
18 triboelectric charging in saltation properly. By combining the results of measurements  
19 and modelling, we find that although the vertical component of the E-field (i.e. 1-D E-  
20 field) inhibits sand transport, 3-D E-field enhances sand transport substantially.  
21 [Furthermore, the model predicts that 3-D E-field enhances the total mass flux and](#)  
22 [saltation height by up to 20 % and 15 %, respectively.](#) This suggests that a truly 3-D E-  
23 field consideration is necessary if one is to explain precisely how the E-field affects  
24 saltation during dust storms. These results will further improve our understanding of  
25 particle triboelectric charging in saltation and help to provide more accurate  
26 characterizations of sand and dust transport during dust storms.

## 27

## 28 **1. Introduction**

29 Contact or triboelectric charging is a ubiquitous phenomenon in dust events

1 (Harrison et al., 2016; Kok and Renno, 2008; Lacks and Sankaran, 2011; Schmidt et al.,  
2 1998; Zheng et al., 2003). The pioneering electric field (E-field) measurements in dust  
3 storms by W. A. Douglas Rudge showed that the vertical atmospheric E-field was  
4 substantially increased to 5-10 kV m<sup>-1</sup> and reversed its direction (became upward-  
5 pointing) during a severe dust storm (Rudge, 1913). Later measurements in dust  
6 storms found downward-pointing (Esposito et al., 2016), upward-pointing (Bo and  
7 Zheng, 2013; Yair et al., 2016; Zhang and Zheng, 2018), and even alternating vertical  
8 E-field which continually reverses direction (Kamra, 1972; Williams et al., 2009), with  
9 the magnitude of up to ~100 kV m<sup>-1</sup>.

10 The significant influences of E-field on the lifting and transport of sand and dust  
11 particles have been verified, both numerically (e.g. Kok and Renno, 2008; Zhang et al.,  
12 2014) and experimentally (e.g. Esposito et al., 2016; Rasmussen et al., 2009). The  
13 effects of E-field on saltation, however, remain obscure. A clear discrepancy between  
14 numerical simulation and field measurement is that: numerical simulation showed a  
15 reduction in saltation mass flux by E-field (e.g. Kok and Renno, 2008; Zheng et al., 2003),  
16 whereas recent field measurements found a dramatic increase in dust concentration  
17 (up to a factor of 10) by E-field (Esposito et al., 2016), suggesting that E-field might  
18 enhance saltation mass flux. This is probably because most previous numerical  
19 simulations only considered the vertical component of the E-field (i.e. 1-D), but there  
20 also in fact exist streamwise and spanwise components of E-field in dust events. For  
21 example, Jackson and Farrell (2006) recorded the horizontal component of the E-field  
22 of up to 120 kV m<sup>-1</sup> in dust devils. Zhang and Zheng (2018) also found the streamwise  
23 and spanwise components (termed horizontal component) of the E-field of up to 150  
24 kV m<sup>-1</sup> in dust storms. Hence, E-field is actually three-dimensional (3-D). In many cases,  
25 the magnitude of the horizontal component is larger than that of the vertical  
26 component. The horizontal component should therefore not be neglected when  
27 evaluating the role of E-field in saltation during dust storms.

28 Most field observations, such as Schmidt et al. (1998) and Bo et al. (2014), studied  
29 the electrical properties of sand particles in dust events. However, these studies are

1 generally not conclusive because the charge transfer between contacting particles are  
2 sensitive to ambient conditions. For example, Schmidt et al. (1998) found that the  
3 mean charge-to-mass ratio of saltating particles at 5 cm height was  $+60 \mu\text{C kg}^{-1}$ , which  
4 did not agree with their finding of upward-pointing vertical E-field. This  
5 inconclusiveness may be attributed to environmental (lurking) factors, such as relative  
6 humidity, soil moisture, surface crust, etc., are not fully controllable (recorded) in the  
7 field observations. The uncertainties in field observations provide motivation for  
8 numerical studies of the particle triboelectric charging in saltation. In addition, unlike  
9 pure saltation (that is, no suspended dust particles), the dust storm is a very complex  
10 dusty phenomenon that is made up by numerous polydisperse particles embedded in  
11 a high Reynolds-number turbulent flow. Such high complexity of dust storms  
12 challenges the accurate simulation of 3-D E-field in dust storms. It is therefore more  
13 straightforward to characterize 3-D E-field experimentally.

14 In this study, we evaluate the effects of 3-D E-field on saltation during dust storms  
15 by combining measurements and modelling. To reveal the properties of 3-D E-field, we  
16 simultaneously measured the 3-D E-fields in the sub-meter layer from 0.05 to 0.7 m  
17 above the ground during a dust storm. Such vertical profile of the 3-D E-field in the  
18 sub-meter layer has not been previously characterized. To reveal how 3-D E-field  
19 affects saltation, we develop a comprehensive numerical model of particle  
20 triboelectric charging in saltation. In this model, the charge transfers between  
21 contacting particles are explicitly calculated, but the 3-D E-field is formulated directly  
22 based on the data measured in our measurements, due to its huge challenges in  
23 modelling. The effects of various important parameters, such as the density of charged  
24 species and the [height-averaged time-varying mean of the 3-D E-field](#), are also  
25 investigated and described herein.

26

## 27 **2. Field campaign**

### 28 **2.1 Observational set-up and uncertainty**

29 We performed 3-D E-field measurements at the Qingtu Lake Observation Array

1 (QLOA) site (approximately  $39^{\circ}12'27''$  N,  $103^{\circ}40'03''$  E, as shown in Fig. 1a), in  
2 May 2014. The measured physical quantities include: wind velocities at four heights  
3 measured by the sonic anemometers (CSAT3B, Campbell Scientific, Inc.) with 50 Hz  
4 sampling frequency; number of saltating particle passing through the measurement  
5 area ( $2\text{ mm}\times 25\text{ mm}$ ) per second at 6 heights measured by sand particle counter (SPC-  
6 91, Niigata Electric Co., Ltd.) with 1 Hz sampling frequency, thus providing an  
7 estimation of the size distribution of saltating particles, saltation mass flux, and  
8 saltation height (Text S1 in the Supplement); 3-D E-field at five heights measured by  
9 the vibrating-reed E-field mill (VREFM, developed by Lanzhou University) with 1 Hz  
10 sampling frequency. The layout of all instruments is shown in Fig. 1b. All instruments  
11 are powered by solar panels. The detailed descriptions of the QLOA site and VREFM  
12 sensor can be found in our previous studies (e.g. Zhang et al., 2017; Zheng, 2013).

13 The measurement uncertainties in our field campaign are threefold: wind velocity  
14 (CSAT3B), particle mass flux (SPC-91), and E-field (VREFM). The CSAT3B is factory  
15 calibrated with an accuracy of  $\pm 8\text{ cm s}^{-1}$ . The SPC-91 is factory calibrated by a set of  
16 filamentation wires of equivalent diameters from 0.138 to 0.451 mm, with an  
17 uncertainty of  $\pm 0.015\text{ mm}$ . The VREFM used in the field measurements is carefully  
18 calibrated and selected in our lab by a parallel-plate E-field calibrator (Zhang et al.,  
19 2017), and its maximum uncertainties range from  $\sim 1.38\%$  to  $\sim 2.24\%$  (see Text S2 in  
20 the Supplement).

21

## 22 **2.2 Data analysis**

23 In general, the actual wind direction exits a specific angle from the prevailing wind  
24 direction. A projection step is therefore needed to obtain the streamwise E-field,  $E_1$ ,  
25 and spanwise E-field,  $E_2$ . For example,  $E_1$  is equal to the sum of the projection of the  
26 measured  $E_x$  and  $E_y$  (E-field in the direction of  $x$  and  $y$  axes, as shown in Fig. 1b)  
27 to the streamwise wind direction.

28 After completing the projection step, we then perform the following steps  
29 sequentially to reveal the pattern of 3-D E-field in the sub-meter layer: (1) estimating

1 time-varying mean values of E-field; (2) computing height-averaged time-varying mean  
2 in the measurement region from 0.05 to 0.7 m above the ground; (3) normalizing E-  
3 field by height-averaged mean values; and (4) finally fitting the vertical profiles of  
4 normalized E-field by the 3-order polynomial functions. It is worth noting that the  
5 measured time series in dust storms are generally non-stationary when viewed as a  
6 whole (e.g. Zhang and Zheng, 2018). In such cases, the statistical values are time-  
7 varying. Here, we use the discrete wavelet transform (DWT) method (Daubechies,  
8 1990) and the ensemble empirical mode decomposition (EEMD) method (Wu and  
9 Huang, 2009), which are widely used in various geophysical studies (e.g. Grinsted et  
10 al., 2004; Huang and Wu, 2008; Wu et al., 2011), to estimate the time-varying mean  
11 values of the measured non-stationary 3-D E-field data. We select these two methods  
12 since the DWT with higher orders of Daubechies wavelet (e.g. db10) and the EEMD can  
13 extract a reasonable and physically meaningful time-varying mean (Su et al., 2015).  
14 Each step for revealing the 3-D E-field pattern is described in detail as follows:

15 The DWT uses a set of mutually orthogonal wavelet basis functions, which are  
16 dilated, translated and scaled versions of a mother wavelet, to decompose an E-field  
17 series  $E(t, z)$  into a series of successive octave band components (Percival and  
18 Walden, 2000), i.e.,

19

$$20 \quad E(t, z) = \sum_{i=1}^N \psi_i(t, z) + \chi_N(t, z) \quad (1)$$

21

22 Where  $N$  is the total number of decomposition levels,  $\psi_i(t, z)$  denotes the  $i$ -th  
23 level wavelet detail component, and  $\chi_N(t, z)$  represents the  $N$ -th level wavelet  
24 approximation (or smooth) component. As  $N$  increases, the frequency contents  
25 become lower and thus the  $N$ -th level approximation component could be regarded  
26 as the time-varying mean values (e.g. Percival and Walden, 2000; Su et al., 2015). In  
27 this study, the DWT decomposition is performed with the Daubechies wavelet of order  
28 10 (db10) at level 10, and thus the 10-th order approximation component can be

1 defined as the time-varying mean:

2

$$3 \quad \bar{E}(t, z) = \chi_{10}(t, z) \quad (2)$$

4

5 which reflect the averages of the  $E(t, z)$  series over a scale of  $2^{10}$  s (about 17.1  
6 minutes).

7 On the other hand, according to the empirical mode decomposition (EMD)  
8 method, the time series  $E(t, z)$  can be decomposed as (Huang et al., 1998)

9

$$10 \quad E(t, z) = \sum_{i=1}^N \xi_i(t, z) + \eta_N(t, z) \quad (3)$$

11

12 through a sifting process, where  $\xi_i(t, z)$  ( $i = 1, 2, \dots, N$ ) are the intrinsic mode  
13 functions (IMFs), and  $\eta_N(t, z)$  is a residual (which is the overall trend or mean). To  
14 reduce the end effects and mode mixing in EMD, the EEMD method is proposed by Wu  
15 and Huang (2009). In EEMD, a set of white noise series,  $w_j(t, z)$  ( $j = 1, 2, \dots, N_e$ ), are  
16 added to the original signal  $E(t, z)$ . Then, each noise-added series is decomposed into  
17 IMFs followed by the same sifting process as in EMD. Finally, the  $i$ -th EEMD  
18 component is defined as the ensemble mean of the  $i$ -th IMFs of the total of  $N_e$   
19 noise-added series (see Wu and Huang, 2009 for details).

20 In this study, the time-varying mean values  $\bar{E}(t, z)$  can be alternatively defined  
21 as the sum of the last four EEMD components,  $\xi_{10}(t, z)$  to  $\xi_{13}(t, z)$ , and the residual,  
22  $\eta_{13}(t, z)$ , i.e.

23

$$24 \quad \bar{E}(t, z) = \sum_{i=10}^{13} \xi_i(t, z) + \eta_{13}(t, z) \quad (4)$$

25

26 which is approximately the 17.3 minutes (very close to the timescale of  $\sim 17.1$  minutes  
27 used in DWT) or longer timescale variability trend (Wu et al., 2011), because the

1 maximum mean frequency of the last four EEMD components is  $5.78 \times 10^{-2}$  Hz (see Figs.  
 2 S5 and S6 in the Supplement for details).

3 According to the above definitions, the time-varying mean can be obtained by the  
 4 DWT and EEMD methods over the timescale of about 17 minutes. As an example, Fig.  
 5 2 shows the results of db10 DWT analysis (Fig. 2b) and EEMD decompositions (Fig. 2c)  
 6 for an E-field time series  $E(t, z)$  in our field campaign. It can be seen that DWT and  
 7 EEMD can properly capture the time-varying mean over the timescale of 17 minutes,  
 8 with very little difference between the two methods.

9 Since the 3-D E-field are measured at five heights in our field campaign, we thus  
 10 define the height-averaged time-varying mean values as

11

$$12 \quad \langle \overline{E}_i(t, z) \rangle = \left| \frac{1}{(0.7 - 0.05)} \int_{0.05}^{0.7} \overline{E}_i(t, z) dz \right| \quad (5)$$

13

14 in the range of 0.05 to 0.7 m height, in order to normalize the E-field data by a unified  
 15 quantity. Further, the E-field data can be normalized as

16

$$17 \quad E_i^+(t, z) = \frac{E_i(t, z)}{\langle \overline{E}_i(t, z) \rangle} \quad (6)$$

18

19 Additionally, to obtain the dimensionless vertical profile of 3-D E-field, the height  $z$   
 20 should also be a dimensionless parameter. Here, the dimensionless height  $z^+$  is  
 21 defined as the ratio of height  $z$  to the mean saltation height  $\bar{z}_{salt}$  during the whole  
 22 observed dust storm, i.e.

23

$$24 \quad z^+ = \frac{z}{\bar{z}_{salt}} \quad (7)$$

25

26 where the saltation height  $z_{salt}$  during a certain time interval is defined as the height  
 27 below which 99 % of the total mass flux is present and can be estimated based on the



1 measured SPC-91 data (see Text S1 in the Supplement for details).

2 Finally, the dimensionless vertical profiles of 3-D E-field at different periods are  
3 **together** fitted by the 3-order polynomial functions:

$$4 \quad E_i^+(z^+) = a_{0,i} + a_{1,i}z^+ + a_{2,i}(z^+)^2 + a_{3,i}(z^+)^3, \quad i = 1,2,3 \quad (8)$$

6  
7 where  $i = 1, 2,$  and  $3$  correspond to the streamwise, spanwise, and vertical  
8 components, respectively.

### 9 10 **3. Saltation model**

11 For modelling steady-state saltation, there are four primary processes, including  
12 (1) particle saltating motion, (2) particle-particle midair collisions, (3) particle-bed  
13 collisions, and (4) particle-wind momentum coupling (Dupont et al., 2013; Kok and  
14 Renno, 2009). Also, the changes in both momentum and electrical charge of each  
15 particle are taken into account in the particle-particle midair and particle-bed collisions.  
16 To avoid overestimating midair collisions in 2-D simulation (Carneiro et al., 2013), we  
17 simulate saltation trajectories in a real 3-D domain. We use the discrete element  
18 method (DEM), which explicitly simulates each particle motion and describes the  
19 collisional forces between colliding particles encompassing normal and tangential  
20 components, to advance the evaluation of the effects of particle midair collisions. In  
21 the following subsections, we will describe each process in detail.

#### 22 23 **3.1 Size distribution of particle sample**

24 Granular materials in natural phenomena, such as sand, aerosols, pulverized  
25 material, seeds of crops, etc., are made up of discrete particles with a wide range of  
26 sizes ranging from a few micrometers to millimeters. The log-normal distribution is  
27 generally used to approximate the size distribution of the sand sample (Dupont et al.,  
28 2013; Marticorena and Bergametti, 1995). Thus, the mass distribution function of a  
29 sand sample with two parameters, average diameter  $d_m$ , and geometric standard

1 deviation  $\sigma_p$ , can be written as

2

$$3 \quad \frac{dM(d_p)}{d\ln(d_p)} = \frac{1}{\sqrt{2\pi}\ln(\sigma_p)} \exp\left\{-\frac{[\ln(d_p) - \ln(d_m)]^2}{2[\ln(\sigma_p)]^2}\right\} \quad (9)$$

4

### 5 **3.2 Equations of saltating particles motion**

6 The total force acting on a saltating particle consists of three distinct interactions  
 7 (Minier, 2016). The first one refers to the wind-particle interaction, which is dominated  
 8 by the drag force with lifting forces such as Saffman force and Magnus force being of  
 9 secondary importance (Dupont et al., 2013; Kok and Renno, 2009). The second  
 10 interaction refers to the particle-particle collisional forces or cohesion caused by  
 11 physical contact between particles. Such interparticle collisional forces can be  
 12 described as a function of the overlaps between the colliding particles. The third  
 13 interaction refers to the forces due to external fields such as gravity and E-field. In this  
 14 study, in addition to the drag force, we also take into account the Magnus force  
 15 because of the remarkable rotation of saltating particles on the order of 100-1000 rev  
 16 s<sup>-1</sup> (Xie et al., 2007). The effects of electrostatic forces on particle motion, which are  
 17 significant for large wind velocity (Schmidt et al., 1998; Zheng et al., 2003), are also  
 18 taken into account. Consequently, the full governing equations of saltating particles  
 19 can be written as

20

$$21 \quad m_{p,i} \frac{d\vec{u}_{p,i}}{dt} = \vec{F}_i^d + \vec{F}_i^m + \sum_j (\vec{F}_{ij}^n + \vec{F}_{ij}^t) + m_i \vec{g} + \zeta_{p,i} \vec{E} \quad (10a)$$

$$22 \quad I_i \frac{d\vec{\omega}_{p,i}}{dt} = \vec{M}_i^{w-p} + \sum_j (\vec{M}_{ij}^c + \vec{M}_{ij}^r) \quad (10b)$$

23

24 where  $m_{p,i}$  is the mass of the  $i$ -th particle;  $\vec{u}_{p,i}$  is the velocity of the particle;  $\vec{F}_i^d$  is  
 25 the drag force;  $\vec{F}_i^m$  is the Magnus force;  $\vec{F}_{ij}^n$  and  $\vec{F}_{ij}^t$  are the normal and tangential  
 26 collisional forces from the  $j$ -th particle, respectively;  $\vec{g}$  is the gravitational

1 acceleration;  $\zeta_{p,i}$  is the charge-to-mass ratio of the sand particles and will be altered  
 2 during every collision (see section 3.4);  $\vec{E}$  is the 3-D E-field given by our  
 3 measurements;  $I_i$  is the moment of inertia;  $\vec{\omega}_{p,i}$  is the angular velocity of the  
 4 particle;  $\vec{M}_i^{w-p}$  is the torque caused by the wind on the particle;  $\vec{M}_{ij}^c$  and  $\vec{M}_{ij}^r$  are  
 5 the tangential torque due to the tangential component of the particle collisional forces  
 6 and the rolling resistance torque, respectively. The summation  $\Sigma$  represents  
 7 considering all particles that are in contact with the  $i$ -th particle.

8

### 9 **3.2.1 Wind-particle interactions**

10 In the absence of saltating particles, the mean wind profile over a flat and  
 11 homogeneous surface is well approximated by the log-law (Anderson and Haff, 1988)

12

$$13 \quad u_m(z) = \frac{u_*}{\kappa} \ln \frac{z}{z_0} \quad (11)$$

14

15 where  $u_m$  is the mean streamwise wind speed;  $z$  is the height above the surface;  
 16  $u_*$  is the friction velocity;  $\kappa \approx 0.41$  is the von Kármán constant;  $z_0$  is the  
 17 aerodynamic roughness, which varies substantially from different flow conditions and  
 18 can be approximately estimated as  $d_m/30$  for the aeolian saltation on Earth (e.g.  
 19 Carneiro et al., 2013; Kok et al., 2012). In the presence of saltation, due to the  
 20 momentum coupling between the saltating particles and wind flow, the modified wind  
 21 speed gradient can be written as (e.g. Kok and Renno, 2009; Pähtz et al., 2015)

22

$$23 \quad \frac{du_m(z)}{dz} = \frac{u_*}{\kappa z} \sqrt{1 - \frac{\tau_p(z)}{\rho_a u_*^2}} \quad (12)$$

24

25 where  $\rho_a$  is the air density,  $\tau_p(z)$  is the particle momentum flux and can be  
 26 numerically determined by (Carneiro et al., 2013; Shao, 2008)

27

$$\tau_p(z) = -\frac{\sum m_{p,i} u_{p,i} w_{p,i}}{L_x L_y \Delta z} \quad (13)$$

with  $L_x$ ,  $L_y$ , and  $\Delta z$  being the streamwise-, spanwise-width of the computational domain, and vertical grid size, respectively;  $u_{p,i}$  and  $w_{p,i}$  are the streamwise and vertical components of particle velocity. The summation in Eq. (13) is performed on the particles located in the range of  $[z, z + \Delta z]$ . Once saltating particle trajectories are known, the wind profile can be determined through integrating Eq. (12) with the no-slip boundary condition  $u_m = 0$  at  $z = z_0$ .

Since sand particles are much heavier than the air and are well smaller than the Kolmogorov scales, the drag force is the dominant force affecting particle motion, which is expressed by (Anderson and Haff, 1991)

$$\vec{F}_i^d = -\frac{\pi d_p^2}{8} \rho_a C_d \vec{u}_r |\vec{u}_r| \quad (14)$$

where  $d_p$  is the diameter of the particle;  $C_d$  is the drag coefficient; and  $\vec{u}_r = \vec{u}_p - \vec{u}_w$  is the particle-to-wind relative velocity. The drag coefficient  $C_d$  is a function of the particle Reynolds number,  $Re_p = \rho_a |\vec{u}_r| d_p / \mu$ , where  $\mu$  is the dynamic viscosity of the air. We calculate the drag coefficient by an empirical relation  $C_d = \left[ (32/Re_p)^{2/3} + 1 \right]^{3/2}$ , which is applicable to the regimes from Stokes flow  $Re_p \ll 1$  to high Reynolds number turbulent flow (Cheng, 1997).

Additionally, we also account for the effects of particle rotation on particle motion using the Magnus force expressed as (Anderson and Hallet, 1986; Loth, 2008; White and Schulz, 1977)

$$\vec{F}_i^m = \frac{\pi d_p^2}{8} \rho_a C_m (\vec{\omega}_{p,i} \times \vec{u}_r) \quad (15)$$

where  $C_m$  is a normalized spin lift coefficient depended on the particle Reynolds

1 number and the circumferential speed of the particle. The torque acting on a particle  
 2 caused by wind flow is calculated from (Anderson and Hallet, 1986; Kok and Renno,  
 3 2009; Shao, 2008)

$$4 \quad \vec{M}_i^{w-p} = \pi \mu d_i^3 \left( \frac{1}{2} \frac{du_m}{dz} - \vec{\omega}_i \right) \quad (16)$$

### 7 **3.2.2 Particle-particle midair collisions**

8 Under moderate conditions, saltation is a dilute flow in which the particle-particle  
 9 collisions are negligible. However, as wind velocity increases, midair collisions become  
 10 increasingly pronounced, especially in the near-surface region. For spherical particles,  
 11 one of the most commonly-used collisional force model is the nonlinear viscoelastic  
 12 model, consisting of two components, i.e. elastic and viscous forces (Brilliantov et al.,  
 13 1996; Haff and Anderson, 1993; Silbert et al., 2001; Tuley et al., 2010).

14 Considering two spherical particles  $i$  and  $j$  with diameters  $d_i$  and  $d_j$ , and  
 15 position vectors  $\vec{x}_i$  and  $\vec{x}_j$ , are in contact with each other. The relative velocity  $\vec{v}_{ij}$   
 16 at the contact point and its normal and tangential components,  $\vec{v}_{ij}^n$  and  $\vec{v}_{ij}^t$ , are  
 17 respectively defined as (Norouzi et al., 2016; Silbert et al., 2001)

$$18 \quad \vec{v}_{ij} = \vec{u}_{p,i} - \vec{u}_{p,j} + 0.5(d_i \vec{\omega}_{p,i} + d_j \vec{\omega}_{p,j}) \times \vec{n}_{ij} \quad (17a)$$

$$19 \quad \vec{v}_{ij}^n = (\vec{v}_{ij} \cdot \vec{n}_{ij}) \vec{n}_{ij} \quad (17b)$$

$$20 \quad \vec{v}_{ij}^t = \vec{v}_{ij} - \vec{v}_{ij}^n \quad (17c)$$

21  
 22  
 23 where  $\vec{n}_{ij} = (\vec{x}_j - \vec{x}_i) / |\vec{x}_j - \vec{x}_i|$  is the unit vector in the direction from the center  
 24 of particle  $i$  point toward the center of particle  $j$ . Suppose that these colliding  
 25 particles having identical mechanical properties with Young's modulus  $Y$ , shear  
 26 modulus  $G$ , and Poisson's ratio  $\nu$ , and thus the normal collisional force can be  
 27 calculated by (Brilliantov et al., 1996; Silbert et al., 2001)

1

2

$$\vec{F}_{ij}^n = -\frac{4}{3}Y^*\sqrt{R^*}\delta_n^{3/2}\vec{n}_{ij} - 2\sqrt{\frac{5}{6}m^*S_n\beta v_n}\vec{n}_{ij} \quad (18)$$

3

4

where  $Y^* = Y/2/(1 - \nu^2)$  is the equivalent Young's modulus;  $\delta_n = 0.5(d_i + d_j) -$

5

$|\vec{x}_i - \vec{x}_j|$  is the normal overlap;  $m^* = m_i m_j / (m_i + m_j)$  is the equivalent particle

6

mass;  $S_n = 2Y^*\sqrt{R^*}\delta_n$  is the normal contact stiffness;  $R^* = d_i d_j / 2 / (d_i + d_j)$  is

7

the equivalent particle radius;  $\beta$  is related to the coefficient of restitution  $e_n$  by the

8

relationship  $\beta = \ln e_n / \sqrt{(\ln e_n)^2 + \pi^2}$ ; and  $v_n = \vec{v}_{ij} \cdot \vec{n}_{ij}$ . The first term on the right-

9

hand side of Eq. (18) represents the elastic force described by Hertz's theory, and the

10

second term represents the viscous force reflecting the inelastic collisions between

11

sand particles. Similarly, the tangential collisional force, which is limited by the

12

Coulomb friction, is given as (Brilliantov et al., 1996; Silbert et al., 2001)

13

$$\vec{F}_{ij}^t = \begin{cases} -8G^*\sqrt{R^*}\delta_t\vec{t}_{ij} - 2\sqrt{\frac{5}{6}m^*S_t\beta v_t}\vec{t}_{ij}, & \text{if } |\vec{F}_{ij}^t| \leq \gamma_s |\vec{F}_{ij}^n| \\ -\gamma_s |\vec{F}_{ij}^n| \vec{t}_{ij}, & \text{if } |\vec{F}_{ij}^t| > \gamma_s |\vec{F}_{ij}^n| \end{cases} \quad (19)$$

15

16

where  $G^* = G/2/(2 - \nu)$  is the equivalent shear modulus;  $\delta_t$  is the tangential

17

overlap;  $\vec{t}_{ij} = \vec{v}_{ij}^t / |\vec{v}_{ij}^t|$  is the tangential unit vector at the contact point;  $S_t =$

18

$8G^*\sqrt{R^*}\delta_n$  is the tangential stiffness;  $v_t = \vec{v}_{ij} \cdot \vec{t}_{ij}$ ; and  $\gamma_s$  is the coefficient of static

19

friction. The torque on the  $i$ -th particle arising from the  $j$ -th particle collisional force

20

is defined as (Haff and Anderson, 1993)

21

22

$$\vec{M}_{ij}^c = 0.5d_i\vec{n}_{ij} \times \vec{F}_{ij}^t \quad (20)$$

23

24

To account for the significant rolling friction, we apply a rolling resistance torque

1 (Ai et al., 2011)

2

$$3 \quad \vec{M}_{ij}^r = -\gamma_r R^* |\vec{F}_{ij}^n| \vec{\omega}_{ij} \quad (21)$$

4

5 on each colliding particle, where  $\mu_r$  is the coefficient of rolling friction, and  $\vec{\omega}_{ij} =$   
6  $(\vec{\omega}_{p,i} - \vec{\omega}_{p,j})/|\vec{\omega}_{p,i} - \vec{\omega}_{p,j}|$  is the unit vector of relative angular velocity.

7

### 8 **3.3 Particle-bed collisions**

9 As a saltating particle collides with the sand bed, it has not only a chance to  
10 rebound but also may eject several particles from the sand bed. For simplicity, we use  
11 a probabilistic representation, termed as “splash function”, to describe the particle-  
12 bed interactions quantitatively (Kok et al., 2012; Shao, 2008). Currently, the splash  
13 function is primarily characterized by wind-tunnel and numerical simulations (e.g.  
14 Anderson and Haff, 1991; Haff and Anderson, 1993; Huang et al., 2017; Rice et al.,  
15 1996). The rebounding probability of a saltating particle colliding with the sand bed is  
16 approximately by (Anderson and Haff, 1991)

17

$$18 \quad P_{reb} = 0.95[1 - \exp(-v_{imp})] \quad (22)$$

19

20 where  $v_{imp}$  is the impact speed of the saltating particle. The kinetic energy of the  
21 rebounding particles is taken as  $0.45 \pm 0.22$  of the impact particle (Kok and Renno,  
22 2009). The rebounding angles  $\theta$  and  $\varphi$ , as depicted in Fig. 3a, obey an exponential  
23 distribution with a mean value of  $40^\circ$ , i.e.  $\theta \sim \text{Exp}(40^\circ)$ , and a normal distribution  
24 with parameters  $0 \pm 10^\circ$ , i.e.  $\varphi \sim \text{N}(0^\circ, 10^\circ)$ , respectively (Dupont et al., 2013; Kok  
25 and Renno, 2009).

26 It is reasonable to assume that the number of ejected particles depends on the  
27 impact speed and its cross-sectional area. Thus, the number of ejected particles from  
28 the  $k$ -th particle bin is (Kok and Renno, 2009)

1

2

$$N_k = \frac{0.02}{\sqrt{gD_{250}}} \frac{D_{imp}}{D_{eje}^k} p_k v_{imp} \quad (23)$$

3

4

5

6

7

8

9

10

### 11 3.4 Particle charge exchanges

12

13

14

15

16

17

18

$$\Delta q_{ij} = -e(\rho_h^j S_j - \rho_h^i S_i) \quad (24)$$

19

20

21

22

23

24

25

26

where  $D_{250} = 0.25 \times 10^{-4}$  m is a reference diameter;  $D_{imp}$  and  $D_{eje}^k$  are the diameter of the impact and ejected particles, respectively; and  $p_k$  is the mass fraction of the  $k$ -th particle bin. The speed of the ejected particles obeys an exponential distribution with mean value taken as  $0.6[1 - \exp(-v_{imp}/40/\sqrt{gD_{250}})]$  (Kok and Renno, 2009). Similar to the rebound process, the ejected angles  $\theta$  and  $\varphi$  are assumed to be  $\theta \sim \text{Exp}(50^\circ)$  and  $\varphi \sim \text{N}(0^\circ, 10^\circ)$ .

In this study, the calculation of the charge transfer between sand particle collisions is based on the asymmetric contact model, assuming that the electrons trapped in high energy states on one particle surface can relax to the other particle surface (Hu et al., 2012; Kok and Lacks, 2009). Thus, the net increment of the charge of particle  $i$  after colliding with particle  $j$ ,  $\Delta q_{ij}$ , can be determined by

where  $e = 1.602 \times 10^{-19}$  C is the elementary charge;  $\rho_h^i$  is the density of the electrons trapped in the high energy states on the surface of particle  $i$  (assuming that all particles have an identical initial value  $\rho_h^0$ ), which is modified as  $\rho_{h,i}^{\text{after}} = \rho_{h,i}^{\text{before}} + (\rho_h^j S_j - \rho_h^i S_i)/(\pi d_i^2)$  due to collisions between particle  $i$  and  $j$ ;  $S_i$  is the particle contact area, which can be approximately calculated as a line integral along the contact path  $L_i$  of particle  $i$



$$S_i = 2 \int_{L_i} \sqrt{R^* \delta_n} dl_i \quad (25)$$

2

3 where  $dl_i$  is the differential of the contact length. In general, when two particles are  
 4 in contact with each other, the relative sliding motion between the two particles  
 5 results in two unequal contact areas  $S_i$  and  $S_j$ , thus producing net charge transfer  
 6  $\Delta q_{ij}$  between the two particles. If the particle's net electrical charge is known, its  
 7 charge-to-mass ratio can be easily determined.

8

### 9 **3.5 Particle-phase statistics**

10 Similar to particle momentum flux (i.e. Eq. 13), particle horizontal mass flux  $q$ ,  
 11 total mass flux  $Q$ , mean particle mass concentration  $m_c$ , and mean particle  
 12 horizontal speed  $\langle u_p \rangle$  can be numerically determined by (Carneiro et al., 2013;  
 13 Dupont et al., 2013)

14

$$q(z) = \frac{\sum m_{p,i} u_{p,i}}{L_x L_y \Delta z} \quad (26a)$$

$$Q = \frac{\sum m_{p,i} u_{p,i}}{L_x L_y} \quad (26b)$$

$$m_c(z) = \frac{\sum m_{p,i}}{L_x L_y \Delta z} \quad (26c)$$

$$\langle u_p \rangle(z) = \frac{\sum u_{p,i}}{L_x L_y \Delta z} \quad (26d)$$

19

20 where the summation  $\sum$  is performed over the saltating particles located in the range  
 21 of  $[z, z + \Delta z]$  for  $q$ ,  $m_c$ , and  $\langle u_p \rangle$ , but it is performed over all saltating particles for  
 22  $Q$ .

23

### 24 **3.6 Model implementation**

1 We consider polydisperse soft-spherical sand particles having log-normal mass  
2 distribution in a 3-D computational domain 0.5 m×0.1 m×1.0 m (as shown in Fig. 3a),  
3 with periodic boundary condition in the  $x$  and  $y$  directions. Here, the upper  
4 boundary is set to be high enough so that the particle escapes from the upper  
5 boundary can be avoided. To reduce the computational cost, the spanwise dimension  
6 is chosen as  $L_y = 0.1$ , since the saltating particles are mainly moving along the  
7 streamwise direction.

8 As shown in Fig. 3b, the model is initiated by randomly releasing 100 uncharged  
9 particles, within the region below 0.3 m, and then such released particles begin to  
10 move under the action of the initial log-law wind flow, triggering saltation through a  
11 series of particle-bed collisions. We use cell-based collision searching algorithms,  
12 which perform collision search for particles located in the target cell and its  
13 neighboring cells, to find the midair colliding pairs. The random processes, particle-  
14 bed collisions described previously, are simulated using a general method called the  
15 inverse transformation. The particle motion and wind flow equations are integrated by  
16 predictor-corrector method AB3AM4; that is, 3-order Adams-Bashforth method to  
17 perform prediction and 4-order Adams-Moulton method to perform the correction.  
18 One of the main advantages of using such multi-step integration method is that the  
19 accuracy of results is not sensitive to the detection of exact moments of collision (Tuley  
20 et al., 2010). The charge transfer between the colliding pairs is caused by their  
21 asymmetric contact and can be determined by Eqs. (24) and (25). When calculating  
22 particle-bed charge transfer, the bed is regarded as an infinite plane. According to the  
23 law of charge conservation, the surface charge density of the infinite bed plane and  
24 the newly ejected particles,  $\sigma$ , is (Kok and Renno, 2008; Zhang et al., 2014)

$$\sigma = - \int_{z_0}^{+\infty} \rho_c(z) dz \quad (27)$$

27  
28 where  $\rho_c$  is the space charge density. For modelling pure saltation, the E-field is

1 calculated by Gauss's law (e.g. Zhang et al., 2014). For modelling saltation during dust  
2 storms, the 3-D E-field is directly formulated by Eq. (8) based on our field  
3 measurements, as mentioned above. The variables used in this study are listed and  
4 described in Table 1.

5

## 6 **4. Results**

### 7 **4.1. Vertical profiles of 3-D E-field**

8 On May 6, 2014, field measurements began at ~12:00 due to the limited power  
9 supply by solar panels. As shown in Fig. 4, although the early stage of dust storm has  
10 not been observed, we successfully recorded data of about 8 hours, which is  
11 substantial enough to reveal the pattern of 3-D E-field. From Fig. 4, it can be seen that,  
12 in general, the streamwise and spanwise components (up to ~80 kV m<sup>-1</sup>) are  
13 consistently larger than the vertical component of the E-field (up to ~40 kV m<sup>-1</sup>). The  
14 vertical profiles of the normalized streamwise, spanwise, and vertical components of  
15 E-field are shown in Figs. 5a-5c, respectively. Note that there is little difference  
16 between the DWT and EEMD results, because these are the mean values over the  
17 ~17.1 and ~17.3 minutes timescales, respectively. To the best of our knowledge, these  
18 data are the first measured 3-D E-field data in the sub-meter layer during dust storms.  
19 Numerous studies showed that the vertical component of E-field in pure saltation  
20 decreased with increasing height (e.g., Kok and Renno, 2008; Schmidt et al., 1998;  
21 Zhang et al., 2014). Interestingly, Fig. 5c shows that during dust storms, all normalized  
22 components,  $E_1^+$  to  $E_3^+$ , decreases monotonically as height increases in the saltation  
23 layer (i.e.  $z^+ \leq 1$ ), similar to the pattern of vertical component in pure saltation.

24 As shown in Figs. 5a-5c, in different periods, each component of the normalized  
25 3-D E-field roughly collapses on a single 3-order polynomial curve (with  $R^2=0.67-0.97$ ,  
26 see Table 2 for details). This suggests that during dust storms, the 3-D E-field in the  
27 sub-meter layer can be characterized as  $\langle \overline{E_i} \rangle E_i^+$ , where  $E_i^+$  represents the pattern  
28 of the dimensionless E-field vertical profile (formulated by Eq. 8), and  $\langle \overline{E_i} \rangle$  represents  
29 the height-averaged time-varying mean defined in Eq. (5). It is worth noting that the

1 E-field pattern  $E_i^+$  and their intensities  $\langle \overline{E_i} \rangle$  are strongly depended on the saltation  
2 conditions, such as dust mass loading, temperature, relative humidity (RH), etc. For  
3 example, at given ambient temperature and RH, the mean E-field intensities  $\langle \overline{E_i} \rangle$   
4 increases linearly with dust mass loading (e.g. Esposito et al., 2016; Zhang et al., 2017).  
5 In addition, both  $E_i^+$  and  $\langle \overline{E_i} \rangle$  could vary from event to event, among them, the  
6 saltation conditions are quite different. So far, a quantitative representation of  $\langle \overline{E_i} \rangle$  is  
7 challenging due to its high complexity, and thus we regard it as a basic parameter in  
8 the following sections for exploring the effects of 3-D E-field on saltation. The fitting  
9 results of Eq. (8) are listed in Table 2, with coefficients as rounded to two decimals. The  
10 formulations of the 3-D E-field can be readily substituted into the numerical model (i.e.  
11 Eq. 10a).

#### 13 **4.2. Effects of particle-particle midair collisions on saltation**

14 Before quantifying the effects of 3-D E-field on saltation by our numerical model,  
15 we draw a comparison of several key physical quantities between the simulated results  
16 and measurements in the case of pure saltation, in order to ensure the convergence  
17 and validity of our numerical code, as shown in Figs. 6a-6c. It is clearly shown that the  
18 saltation eventually reaches a dynamic steady-state after  $\sim 4$  seconds. The number of  
19 the impacting particles ( $\sim 72$  grains) is equal to the sum of the rebounding ( $\sim 50$  grains)  
20 and the ejected particles ( $\sim 22$  grains) during the time interval of  $10^{-4}$  s. At steady-state,  
21 each impacting particle, on average, produces a single saltating particle, either by  
22 rebound or by ejection. As shown in Fig. 6b, the total mass flux is well predicted by our  
23 numerical model, and midair collisions enhance the total mass flux dramatically,  
24 especially for less particle viscous dissipation (i.e. large  $e_n$ ) and large friction velocity.  
25 Also, the predicted charge-to-mass ratios of saltating particles are widely distributed  
26 from  $-400$  to  $+60 \mu\text{C kg}^{-1}$ , consistent with the previous measurements of charge-to-  
27 mass ratio in pure saltation (Bo et al., 2014; Schmidt et al., 1998; Zheng et al., 2003).  
28 In addition to affecting sand transport, midair collisions also affect charge exchanges

1 between saltating particles. When considering midair collisions, the charge-to-mass  
2 ratio distribution shifts slightly toward zero as the wind velocity increases, as shown in  
3 Figs. 7a-7c.

### 4 5 **4.3. Effects of 3-D E-field on saltation**

6 By substituting the formulations of the 3-D E-field (i.e.  $\langle \overline{E}_i \rangle E_i^+$ ,  $i = 1,2,3$ ) into  
7 our model (i.e. Eq. 10a), we then evaluate the effects of 3-D E-field on saltation during  
8 storms properly. As shown in Fig. 8a, compared to the case without E-field, the vertical  
9 component of the E-field (i.e. 1-D E-field) inhibits mass flux, in agreement with  
10 previous studies (Kok and Renno, 2008; Zheng et al., 2003). However, the mass flux is  
11 enhanced by 3-D E-field, causing the simulated value closer to our measured data.  
12 Such enhancement of mass flux by 3-D E-field can be qualitatively explained by the  
13 considerable enhancements of  $m_c$  below  $\sim 0.02$  m height (Fig. 9a) and  $\langle u_p \rangle$  in the  
14 range from 0.01 to 0.1 m height (Fig. 9b), due to the streamwise and spanwise  
15 components. Meanwhile, although the saltation height is not sensitive to E-field  
16 vertical component, 3-D E-field enhances the saltation height significantly and,  
17 therefore, makes the numerical prediction more accurate (Fig. 8b). This is because  
18 when considering the E-field vertical component, the mass flux profile is very similar  
19 to the case of no E-field consideration (Figs. 8a and 9). In contrast, 3-D E-field causes a  
20 distortion of the mass flux profile (as well as  $m_c$  and  $\langle u_p \rangle$ ), and thus alters saltation  
21 height significantly (Figs. 8a and 9).

22 Additionally, we also explore how the key parameter, density of charged species  
23  $\rho_h^0$ , affects saltation, as shown in Figs. 10a-10c. Since the height-averaged time-varying  
24 mean is strongly depended on the ambient conditions such as temperature and RH,  
25 the height-averaged time-varying mean is set at two different levels. The predicted  
26 results show that, at each height-averaged time-varying mean level, the magnitude of  
27 the charge-to-mass ratio increases with increasing  $\rho_h^0$ , and then reaches a relatively  
28 equilibrium value at approximately  $\rho_h^0 = 10^{16}$  m<sup>-2</sup> (Fig. 10a), thus leading to a  
29 constant enhancement of total mass flux  $Q$  and saltation height  $z_{salt}$  (Figs. 10b and

1 10c). For the larger height-averaged time-varying mean, the enhancements of the total  
2 mass flux  $Q$  and saltation height  $z_{salt}$  could exceed 20 % and 15 %, respectively.

## 3 4 **5. Discussion**

### 5 **5.1. Field measurements of 3-D E-field in the sub-meter layer**

6 To determine the effects of particle triboelectric charging on saltation precisely,  
7 3-D E-field measurements in the saltation layer (i.e. sub-meter above the ground) is  
8 required. Although the E-field measurements, such as Bo and Zheng (2013), Esposito  
9 et al. (2016), Kamra (1972), Rudge (1913), Williams et al. (2009), and Zhang et al. (2017)  
10 in dust storms are numerous, 3-D E-field in the sub-meter layer have not been studied  
11 so far. This is because the traditional atmospheric E-field sensors, such as CS110 sensor  
12 manufactured by Campbell Scientific, Inc., have dimensions of  $15.2 \times 15.2 \times 43.2 \text{ cm}^3$   
13 (e.g. Esposito et al., 2016; Yair et al., 2016), which is too large compared to the height  
14 of saltation layer. Thus, it will lead to significant disturbances of the ambient E-field.  
15 Fortunately, the diameter of the VREFM sensor developed by Lanzhou University is  
16 only 2 cm and thus could considerably eliminate the E-field disturbances (Zhang et al.,  
17 2017; Zheng, 2013). In this study, using the VREFM sensors, we have measured and  
18 characterized the 3-D E-field from 0.05 to 0.7 m height during dust storms, which can  
19 provide valuable data for investigating the mechanisms of particle triboelectric  
20 charging in saltation.

21 In E-field data analysis, the E-field is normalized by its time-varying mean over the  
22 timescale of approximately 17 minutes, which can be extracted by the DWT and EEMD  
23 methods with negligible end effects and mode mixing (Percival and Walden, 2000; Wu  
24 and Huang, 2009). At the same time, since the saltation height  $z_{salt}$  slightly varies  
25 with time (i.e.  $0.172 \pm 0.0343 \text{ m}$ , see Fig. S3 in the supplement), the height  $z$  above  
26 the ground is normalized by the mean saltation height  $\bar{z}_{salt}$ . Note that we calculate  
27 the saltation height and mass flux over every 30-min time interval because the  
28 sufficiently long period is needed to capture all scales of turbulence (Martin and Kok,  
29 2017; Sherman and Li, 2012). The 3-D E-field pattern is finally characterized as the 3-

1 order polynomials, but it is only valid in the range that is not too far beyond the  
2 measurement points. Additionally, the 3-D E-field pattern of dust storms may vary  
3 event to event, because it is strongly related to the driving mechanisms of dust storms,  
4 such as monsoon winds, squall lines, and thunderstorms (Shao, 2008), and ambient  
5 conditions, such as temperature and relative humidity (Esposito et al., 2016; Zhang  
6 and Zheng, 2018). Although the 3-D E-field pattern revealed in this study may not be  
7 a universal feature, the proposed E-field data analysis method can be easily applied to  
8 other cases.

## 10 **5.2. An entirely distinct 3-D E-field in the saltation layer during dust storms**

11 Like many previous studies, the E-field can be simplified to 1-D (i.e. vertical  
12 component) in pure saltation (e.g. Kok and Renno, 2008), since in such cases the  
13 magnitude of the streamwise and spanwise components is much less than that of  
14 vertical component (Zhang et al., 2014). However, during dust storms, the streamwise  
15 and spanwise components are consistently larger than the vertical component, as  
16 mentioned previously. E-field is therefore 3-D. In contrast to the vertical component,  
17 which is closely related to the total mass loading (Esposito et al., 2016; Williams et al.,  
18 2009), the intense streamwise and spanwise components are aerodynamically created  
19 due to the nonuniform transport of charged particles in the [streamwise and spanwise](#)  
20 [directions](#) (Zhang et al., 2014). It is well-known that dust storm is a polydisperse  
21 [particle-laden turbulent flow at very high-Reynolds-number \(up to  \$\sim 10^8\$ \)](#). During dust  
22 [storms, the particle transport is regulated by the large- and very-large-scale motions](#)  
23 [of wind flows \(Jacob and Anderson, 2016\)](#), which may lead to the phenomenon that  
24 [the charged particles are more nonuniformly distributed \(over a larger spatial scale\) in](#)  
25 [dust storms than in pure saltation](#).

## 27 **5.3. Particle-particle triboelectric charging resolved model**

28 Although most physical mechanisms, such as asymmetric contact, polarization by  
29 external E-fields, statistical variations of material properties and shift of aqueous ions,

1 are responsible for particle triboelectric charging, contact or triboelectric charging is  
2 the primary mechanism (e.g. Harrison et al., 2016; Lacks and Sankaran, 2011; Zheng,  
3 2013). In previous model, however, the charge-to-mass ratios of the saltating particles  
4 are either assumed to be a constant value (e.g. Schmidt et al., 1998; Zhang et al., 2014;  
5 Zheng et al., 2003), or are not accounted for in the particle-particle midair collisions  
6 (e.g. Kok and Renno, 2008). In this study, by using DEM together with an asymmetric  
7 contact electrification model, we account for the particle-particle triboelectric  
8 charging during midair collisions in saltation. [The DEM implemented by cell-based](#)  
9 [algorithms is effectively to detect and evaluate most of the particle-particle midair](#)  
10 [collisional dynamics \(Norouzi et al., 2016\)](#). Meanwhile, the charge transfer between  
11 colliding particles can be determined by Eqs. (24) and (25). Compared to the previous  
12 studies (e.g. Kok and Lacks, 2009), the main innovation of this model is that the  
13 comprehensive consideration of the particle collisional dynamics affecting particle  
14 charge transfer is involved. In summary, the present model is a particle-particle midair  
15 collision resolved model, and the predicted charge-to-mass ratio agrees well with the  
16 published measurement data (see Fig. 6c). These findings indicate that midair  
17 collisions in saltation are important, both in momentum and charge exchanges.

#### 19 **5.4. Implications for evaluating particle triboelectric charging in dust events**

20 It is generally accepted that E-field could considerably affect the lifting and  
21 transport of sand particles. As the findings of previous 1-D E-field models (e.g. Kok and  
22 Renno, 2008), the E-field has been proven to inhibit sand transport in our model, when  
23 considering the vertical component of the E-field alone. In contrast to the 1-D E-field,  
24 our model further shows that the real 3-D E-field in dust storms enhances sand  
25 transport substantially, consistent with a recent measurement by Esposito et al. (2016).  
26 [This 3-D E-field model may resolve the discrepancy between the 1-D E-field model \(e.g.](#)  
27 [Kok and Renno, 2008\) and the recent measurement \(i.e. Esposito et al., 2016\)](#). In  
28 [addition, the saltation height has also been enhanced by 3-D E-field](#). Therefore, it is  
29 [necessary to consider 3-D E-field in further studies](#).



1            However, a remaining critical challenge is still to simulate particle triboelectric  
2 charging in dust storms precisely. The driving atmospheric turbulent flows having a  
3 typical Reynolds number on the order of  $10^8$  cover a broad range of length and time  
4 scales, which needs huge computational cost to resolve (e.g. Shao, 2008). On the other  
5 hand, particle triboelectric charging is so sensitive to particle's collisional dynamics  
6 that it needs to resolve each particle collisional dynamics (e.g. Hu et al., 2012; Lacks  
7 and Sankaran, 2011). To model the particle's collisional dynamics properly, the time  
8 steps of DEM are generally from  $10^{-7}$  to  $10^{-4}$  s (Norouzi et al., 2016). However, steady-  
9 state saltation motion often requires several seconds to several tens of seconds to  
10 reach the equilibrium state. In this study, when  $u_* = 0.5 \text{ m s}^{-1}$  and the computational  
11 domain is  $0.5 \times 0.1 \times 1.0 \text{ m}^3$ , the total number of saltating particles exceeds  $7 \times 10^4$  (Fig.  
12 S8 in the Supplement). Consequently, the triboelectric charging in saltation is currently  
13 very difficult to simulate, where a large number of polydisperse sand particles, the high  
14 Reynolds-number turbulent flow, and the inter-particle electrostatic forces are  
15 mutually coupled. In the present version of the model, we do not consider the particle-  
16 particle interactions such as particle agglomeration and fragmentation during particle  
17 collision or frictional contact, as well as the particle-turbulence interaction that is the  
18 effects of turbulent fluctuations on the triboelectric charging and dynamics of particles.  
19 Further studies require considerable effort to incorporate these interactions,  
20 especially turbulence, which is very important for large wind velocity.

## 21 22 **6. Conclusions**

23            Severe dust storms occurring in arid and semiarid regions threaten human lives  
24 and result in substantial economic damages. Intense E-field up to  $\sim 100 \text{ kV m}^{-1}$  does  
25 exist in dust storms and could strongly affect particle dynamics. In this study, we  
26 performed the field measurements of 3-D E-field in the sub-meter layer from 0.05 to  
27 0.7 m above the ground during dust storms by VREFM sensors. Meanwhile, by  
28 introducing the DEM and asymmetric charging mechanism into the saltation model,  
29 we numerically study the effects of 3-D E-field on saltation. Overall, our results show

1 that: (1) measured 3-D E-field data roughly collapse on the 3-order polynomial curves  
2 when normalized, providing a simple representation of the 3-D E-field during dust  
3 storms for the first time; (2) the inclusion of 3-D E-field in saltation model may resolve  
4 the discrepancy between previous 1-D E-field model (e.g. Kok and Renno, 2008) and  
5 measurements (Esposito et al., 2016) in the aspect of whether the E-field inhibits or  
6 enhances saltation; (3) midair collisions dramatically affect both momentum and  
7 charge exchanges between saltating particles; and (4) the model predicts that 3-D E-  
8 field enhances the total mass flux and saltation height significantly, suggesting that 3-  
9 D E-field should be considered in future models, especially for dust storms.

10 We have also performed discussions about various sensitive parameters such as  
11 the density of charged species, the coefficient of restitution, and the height-averaged  
12 time-varying mean of the 3-D E-field. These results significantly add new knowledge to  
13 the role of particle triboelectric charging in determining the transport and lifting of  
14 sand and dust particles. A great effort is further needed to understanding the  
15 interactions such as particle agglomeration and fragmentation, as well as the effects  
16 of the turbulence on the triboelectric charging and dynamics of particles.

17

### 18 **Data availability**

19 The E-field data recorded in our field campaign are provided as a CSV file in the  
20 Supplement.

21

### 22 **Author contribution**

23 H.Z. performed the field observations, numerical simulation, and data analyses as  
24 well as wrote the manuscript, which was guided and edited by Y.H.Z. All authors  
25 discussed the results and commented on the manuscript.

26

### 27 **Competing interests**

28 The authors declare that they have no conflict of interest.

29

## 1 Acknowledgments

2 We thank the editor, Markku Kulmala, and two anonymous reviewers for their  
3 comprehensive and insightful comments that greatly improve the final manuscript.

4 This work was supported by the National Natural Science Foundation of China (grant  
5 numbers 11802109 and 11490553), the Young Elite Scientists Sponsorship Program by  
6 CAST (grant number 2017QNRC001), and the Fundamental Research Funds for the  
7 Central Universities (grant number lzujbky-2018-7).

## 9 References

10 Ai, J., Chen, J. F., Rotter, J. M., and Ooi, J. Y.: Assessment of rolling resistance models in  
11 discrete element simulations, *Powder Technol.*, 206, 269–282,  
12 doi:10.1016/j.powtec.2010.09.030, 2011.

13 Anderson, R. S., and Hallet, B.: Sediment transport by wind: toward a general model,  
14 *Geol. Soc. Am. Bull.*, 97, 523-535, doi: 10.1130/0016-  
15 7606(1986)97<523:STBWTA>2.0.CO;2, 1986.

16 Anderson, R. S., and Haff, P. K.: Simulation of eolian saltation, *Science*, 241, 820–823,  
17 doi:10.1126/science.241.4867.820, 1988.

18 Anderson, R. S., and Haff, P. K.: Wind modification and bed response during saltation  
19 of sand in air, *Acta Mech.*, 1, 21–51, doi:10.1007/978-3-7091-6706-9\_2, 1991.

20 Bagnold, R.: *The Physics of Blown Sand and Desert Dunes*, Chapman & Hall, London,  
21 1941.

22 Bo, T. L., Zhang, H., and Zheng, X. J.: Charge-to-mass ratio of saltating particles in wind-  
23 blown sand, *Sci. Rep.*, 4, 5590, doi:10.1038/srep05590, 2014.

24 Bo, T. L., and Zheng, X. J.: A field observational study of electrification with in a dust  
25 storm in Minqin, China, *Aeolian Res.*, 8, 39–47, doi:10.1016/j.aeolia.2012.11.001,  
26 2013.

27 Brilliantov, N. V., Spahn, F., Hertzsch, J. M., and Poschel, T.: Model for collisions in  
28 granular gases, *Phys. Rev. E*, 53, 5382, doi:10.1103/PhysRevE.53.5382, 1996.

29 Carneiro, M. V., Araújo, N. A., Pähtz, T., and Herrmann, H. J.: Midair collisions enhance

1 saltation, *Phys. Rev. Lett.*, 115, 058001, doi:10.1103/PhysRevLett.111.058001,  
2 2013.

3 Cheng, N. S.: Simplified settling velocity formula for sediment particle, *J. Hydraul. Eng.*,  
4 123, 149–152, doi:10.1061/(ASCE)0733-9429(1997)123:2(149), 1997.

5 Dupont, S., Bergametti, G., Marticorena, B., and Simoens, S.: Modeling saltation  
6 intermittency, *J. Geophys. Res.-Atmos.*, 118, 7109–7128, doi:10.1002/jgrd.50528,  
7 2013.

8 Esposito, F., Molinaro, R., Popa, C.I., Molfese, C., Cozzolino, F., Marty, L., Taj-Eddine, K.,  
9 Achille, G. D., Franzese, G., and Silvestro, S.: The role of the atmospheric electric  
10 field in the dust lifting process, *Geophys. Res. Lett.*, 43, 5501–5508,  
11 doi:10.1002/2016GL068463, 2016.

12 [Grinsted, A., Moore, J. C., and Jevrejeva, S.: Application of the cross wavelet transform  
13 and wavelet coherence to geophysical time series, \*Nonlinear Proc. Geoph.\*, 11,  
14 561-566, doi: 10.5194/npg-11-561-2004, 2004.](#)

15 Haff, P. K., and Anderson, R. S.: Grainscale simulations of loose sedimentary beds: the  
16 example of grain-bed impacts in aeolian saltation, *Sedimentology*, 40, 175–198,  
17 doi:10.1111/j.1365-3091.1993.tb01760.x, 1993.

18 Harrison, R. G., Barth, E., Esposito, F., Merrison, J., Montmessin, F., Aplin, K. L., Borlina,  
19 C., Berthelier, J. J., Dprez, G., and Farrell, W. M.: Applications of electrified dust  
20 and dust devil electrostatics to martian atmospheric electricity, *Space Sci. Rev.*,  
21 203, 299–345, doi:10.1007/s11214-016-0241-8, 2016.

22 Hu, W., Xie, L., and Zheng, X.: Contact charging of silica glass particles in a single  
23 collision, *Appl. Phys. Lett.*, 101, 114107, doi:10.1063/1.4752458, 2012.

24 [Huang, H. J., Bo, T. L., and Zhang, R.: Exploration of splash function and lateral velocity  
25 based on three-dimensional mixed-size grain/bed collision. \*Granul. Matter\*, 19\(4\),  
26 73, doi: 10.1007/s10035-017-0759-9, 2017.](#)

27 Huang, N. E., Shen, Z., Long, S. R., Wu, M. C., Shih, H. H., Zheng, Q., Yen, N. C., Tung, C.  
28 C., and Liu, H. H.: The empirical mode decomposition and the Hilbert spectrum  
29 for nonlinear and non-stationary time series analysis, *Proc. R. Soc. A-Math. Phys.*

1 Eng. Sci., 454, 903–995, doi:10.1098/rspa.1998.0193, 1998.

2 Huang, N. E., and Wu, Z.: A review on Hilbert-Huang transform: Method and its  
3 applications to geophysical studies, *Rev. Geophys.*, 46, RG2006,  
4 doi:10.1029/2007RG000228, 2008.

5 Jackson, T. L., and Farrell, W. M.: Electrostatic fields in dust devils: an analog to Mars,  
6 *IEEE Trans. Geosci. Remote Sensing*, 44, 2942–2949,  
7 doi:10.1109/TGRS.2006.875785, 2006.

8 Kamra, A. K.: Measurements of the electrical properties of dust storms, *J. Geophys.*  
9 *Res.*, 77, 5856–5869, doi:10.1029/JC077i030p05856, 1972.

10 Kawamura, R.: Study on sand movement by wind, Technical Report, Institute of Science  
11 and Technology, University of Tokyo, 5, 95–112, 1951.

12 Kok, J. F., and Lacks, D. J.: Electrification of granular systems of identical insulators, *Phys.*  
13 *Rev. E*, 79, 051304, doi:10.1103/PhysRevE.79.051304, 2009.

14 Kok, J. F., Parteli, E. J., Michaels, T. I., and Karam, D. B.: The physics of wind-blown sand  
15 and dust, *Rep. Prog. Phys.*, 75, 106901, doi:10.1088/0034-4885/75/10/106901,  
16 2012.

17 Kok, J. F., and Renno, N. O.: Electrostatics in wind-blown sand, *Phys. Rev. Lett.*, 100,  
18 014501, doi:10.1103/PhysRevLett.100.014501, 2008.

19 Kok, J. F., and Renno, N. O.: A comprehensive numerical model of steady state saltation  
20 (COMSALT), *J. Geophys. Res.-Atmos.*, 114, doi:10.1029/2009JD011702, 2009.

21 Lacks, D. J., and Sankaran, R. M.: Contact electrification of insulating materials, *J. Phys.*  
22 *D-Appl. Phys.*, 44, 453001, doi:10.1088/0022-3727/44/45/453001, 2011.

23 Lettau, K., and Lettau, H. H.: Experimental and micro-meteorological field studies of  
24 dune migration, in Lettau, K., and Lettau, H. H., eds., *Exploring the World's Driest*  
25 *Climate*, Institute for Environmental Studies, University of Wisconsin Madison,  
26 110–147, 1978.

27 Loth, E.: Lift of a spherical particle subject to vorticity and/or spin, *AIAA J.*, 46, 801–  
28 809, doi:10.2514/1.29159, 2008.

29 Marticorena, B., and Bergametti, G.: Modeling the atmospheric dust cycle: 1. design

1 of a soil-derived dust emission scheme, *J. Geophys. Res.-Atmos.*, 100, 16415–  
2 16430, doi:10.1029/95JD00690, 1995.

3 [Martin, R. L., and Kok, J. F.: Wind-invariant saltation heights imply linear scaling of  
4 aeolian saltation flux with shear stress, \*Sci. adv.\*, 3, doi: 10.1126/sciadv.1602569,  
5 2017.](#)

6 Minier, J. P.: Statistical descriptions of polydisperse turbulent two-phase flows, *Phys.*  
7 *Rep.*, 665, 1–122, doi:10.1016/j.physrep.2016.10.007, 2016.

8 Norouzi, H. R., Zarghami, R., Sotudeh-Gharebagh, R., and Mostoufi, N.: Coupled CFD-  
9 DEM modeling: formulation, implementation and application to multiphase flows,  
10 John Wiley & Sons, Chichester, 2016.

11 Owen, P. R.: Saltation of uniform grains in air, *J. Fluid Mech.*, 20, 225–242,  
12 doi:10.1017/S0022112064001173, 1964.

13 Pähtz, T., Omeradžić, A., Carneiro, M. V., Araújo, N. A., and Herrmann, H. J.: Discrete  
14 Element Method simulations of the saturation of aeolian sand transport, *Geophys.*  
15 *Res. Lett.*, 42, 2063–2070, doi:10.1002/2014GL062945, 2015.

16 [Percival, D. B., Walden, A. T.: \*Wavelet methods for time series analysis\*, Cambridge, UK,  
17 Cambridge UP, 2000.](#)

18 Rasmussen, K. R., Kok, J. F., and Merrison, J. P.: Enhancement in wind-driven sand  
19 transport by electric fields, *Planet Space Sci.*, 57, 804–808,  
20 doi:10.1016/j.pss.2009.03.001, 2009.

21 Rice, M. A., Willetts, B. B., and McEwan, I. K.: Observations of collisions of saltating  
22 grains with a granular bed from high-speed cine-film, *Sedimentology*, 43, 21-31,  
23 doi:10.1111/j.1365-3091.1996.tb01456.x, 1996.

24 Rudge, W. A. D.: Atmospheric electrification during South African dust storms, *Nature*,  
25 91, 31–32, doi:10.1038/091031a0, 1913.

26 Schmidt, D. S., Schmidt, R. A., and Dent, J. D.: Electrostatic force on saltating sand, *J.*  
27 *Geophys. Res.-Atmos.*, 103, 8997–9001, doi:10.1029/98JD00278, 1998.

28 Shao, Y. P.: *Physics and Modelling of Wind Erosion*, Springer Science & Business Media,  
29 Heidelberg, 2008.

- 1 Sherman, D. J., and Li, B.: Predicting aeolian sand transport rates: A reevaluation of  
2 models, *Aeolian Res.*, 3, 371-378, doi: 10.1016/j.aeolia.2011.06.002, 2012.
- 3 Silbert, L. E., Ertaş, D., Grest, G. S., Halsey, T. C., Levine, D., and Plimpton, S. J.: Granular  
4 flow down an inclined plane: Bagnold scaling and rheology, *Phys. Rev. E*, 64,  
5 051302, doi:10.1103/PhysRevE.64.051302, 2001.
- 6 Sørensen, M.: On the rate of aeolian transport, *Geomorphology*, 59, 53–62,  
7 doi:10.1016/j.geomorph.2003.09.005, 2004.
- 8 Su, Y., Huang, G., and Xu, Y. L.: Derivation of time-varying mean for non-stationary  
9 downburst winds, *J. Wind Eng. Ind. Aerod.*, 141, 39-48, doi:  
10 10.1016/j.jweia.2015.02.008, 2015.
- 11 Tuley, R., Danby, M., Shrimpton, J., and Palmer, M.: On the optimal numerical time  
12 integration for lagrangian dem within implicit flow solvers, *Comput. Chem. Eng.*,  
13 34, 886–899, doi:10.1016/j.compchemeng.2009.10.003, 2010.
- 14 White, B. R., and Schulz, J. C.: Magnus effect in saltation, *J. Fluid Mech.*, 81, 497–512,  
15 doi:10.1017/S0022112077002183, 1977.
- 16 Williams, E., Nathou, N., Hicks, E., Pontikis, C., Russell, B., Miller, M., and Bartholomew,  
17 M. J.: The electrification of dust-lofting gust fronts (haboobs) in the sahel, *Atmos.*  
18 *Res.*, 91, 292–298, doi:10.1016/j.atmosres.2008.05.017, 2009.
- 19 Wu, Z., and Huang, N. E.: Ensemble empirical mode decomposition: a noise-assisted  
20 data analysis method, *Adv. Adaptive Data Anal.*, 1, 1-41, doi:  
21 10.1142/S1793536909000047, 2009.
- 22 Wu, Z., Huang, N. E., Wallace, J. M., Smoliak, B. V., and Chen, X.: On the time-varying  
23 trend in global-mean surface temperature, *Clim. Dyn.*, 37, 759–773,  
24 doi:10.1007/s00382-011-1128-8, 2011.
- 25 Xie, L., Ling, Y., and Zheng, X.: Laboratory measurement of saltating sand particles’  
26 angular velocities and simulation of its effect on saltation trajectory, *J. Geophys.*  
27 *Res.-Atmos.*, 112, D12116, doi:10.1029/2006JD008254, 2007.
- 28 Yair, Y., Katz, S., Yaniv, R., Ziv, B., and Price, C.: An electrified dust storm over the Negev  
29 desert, *Israel, Atmos. Res.*, 181, 63–71, doi:10.1016/j.atmosres.2016.06.011,

1           2016.

2   Zhang, H., Bo, T. L., and Zheng, X.: Evaluation of the electrical properties of dust storms  
3           by multi-parameter observations and theoretical calculations, *Earth Planet. Sci.*  
4           *Lett.*, 461, 141–150, doi:10.1016/j.epsl.2017.01.001, 2017.

5   Zhang, H., and Zheng, X.: Quantifying the large-scale electrification equilibrium effects  
6           in dust storms using field observations at Qingtu Lake Observatory, *Atmos. Chem.*  
7           *Phys.*, 18, 17087–17097, doi:10.5194/acp-18-17087-2018, 2018.

8   Zhang, H., Zheng, X. J., and Bo, T. L.: Electrification of saltating particles in wind-blown  
9           sand: Experiment and theory, *J. Geophys. Res.-Atmos.*, 118, 12,086-12,093.  
10          doi:10.1002/532 2013JD020239, 2013.

11   Zhang, H., Zheng, X. J., and Bo, T. L.: Electric fields in unsteady wind-blown sand, *Eur.*  
12          *Phys. J. E*, 37, 13, doi:10.1140/epje/i2014-14013-6, 2014.

13   Zheng, X. J.: Electrification of wind-blown sand: recent advances and key issues, *Eur.*  
14          *Phys. J. E*, 36, 138, doi:10.1140/epje/i2013-13138-4, 2013.

15   Zheng, X. J., Huang, N., and Zhou, Y. H.: Laboratory measurement of electrification of  
16          wind-blown sands and simulation of its effect on sand saltation movement, *J.*  
17          *Geophys. Res.-Atmos.*, 108, doi:10.1029/2002JD002572, 2003.

18



1 **Table 1.** Description of all variables used in this study.

Symbols	Physical meaning	Units
$a_{0,i}, a_{1,i}, a_{2,i}, a_{3,i}$	fitting coefficients in Eq. (8)	1
$C_d$	drag coefficient	1
$C_m$	normalized spin lift coefficient in Magnus force formula	1
$d_p$	particle diameter	m
$d_i, d_j$	diameters of particle $i$ and $j$	m
$d_m$	mean diameter of particle sample in the numerical model	m
$D_{imp}, D_{ej}^k$	diameter of the impact and ejected particles	m
$e_n$	coefficient of restitution of particles	1
$E(t, z)$	a time series of measured E-field	kV m <sup>-1</sup>
$\bar{E}(t, z)$	time-varying mean values of $E(t)$	kV m <sup>-1</sup>
$\langle \bar{E}_i(t, z) \rangle$	height-averaged time-varying mean values of $E(t)$	kV m <sup>-1</sup>
$E_i^+(z^+)$	dimensionless E-field of component $i$	1
$E_1, E_2, E_3$	streamwise, spanwise, and vertical components of E-field	kV m <sup>-1</sup>
$\vec{F}_i^d, \vec{F}_i^m$	drag force and Magnus force acting on particle $i$	N
$\vec{F}_{ij}^d, \vec{F}_{ij}^t$	the normal and tangential collisional forces	N
$g=9.81$	gravitational acceleration	m s <sup>-2</sup>
$G$	shear modulus of particles	Pa
$G^*$	equivalent shear modulus between two contacting particles	Pa
$I_i$	moment of inertia of particle $i$	kg m <sup>2</sup>
$L_x, L_y$	streamwise and spanwise width of the computational domain	m
$m^*$	equivalent particle mass between two contacting particles	kg
$m_{p,i}$	mass of particle $i$	kg
$m_c$	mean particle mass concentration	kg m <sup>-3</sup>
$\vec{M}_i^{w-p}, \vec{M}_{ij}^c, \vec{M}_{ij}^r$	torque due to the wind, the torque due to the tangential component of the particle collisional forces, and the rolling resistance torque	N·m
$\vec{n}_{ij}$	unit vector in the direction from the center of particle $i$ point toward the center of particle $j$	-
$N$	number of the decomposition levels of DWT and EEMD	1
$N_e$	number of white noise series added to the original E-field series	1
$N_k$	number of ejected particles from the $k$ -th particle bin	1
$p_k$	mass fraction of the $k$ -th particle bin	1
$P_{reb}$	rebouncing probability of a saltating particle colliding with the sand bed	1
$q, Q$	mass flux and total mass flux defined in Eq. (26)	kg m <sup>-2</sup> s <sup>-1</sup> , Kg m <sup>-1</sup> s <sup>-1</sup>
$R^*$	equivalent particle radius between two contacting particles	m
$Re_p$	particle Reynolds number	1
$S_i, S_j$	contact area of particle $i$ and $j$	m <sup>2</sup>
$\vec{u}_r$	particle-to-wind relative velocity	m s <sup>-1</sup>
$u_m$	mean streamwise wind speed	m s <sup>-1</sup>
$u_*$	friction velocity	m s <sup>-1</sup>

**Table 1.** Continued.

Symbols	Physical meaning	Units
$\vec{u}_{p,i}$	velocity of particle $i$	$\text{m s}^{-1}$
$u_{p,i}, w_{p,i}$	streamwise and vertical components of particle velocity	$\text{m s}^{-1}$
$\langle u_p \rangle$	mean particle horizontal speed	$\text{m s}^{-1}$
$v_{imp}$	impact speed of the saltating particle	$\text{m s}^{-1}$
$\vec{v}_{ij}, \vec{v}_{ij}^n, \vec{v}_{ij}^t$	relative velocity between particle $i$ and $j$ at the contact point, and its normal and tangential components	$\text{m s}^{-1}$
$\vec{x}_i, \vec{x}_j$	position vectors of particle $i$ and $j$	$\text{m}$
$Y=10^8$	Young's modulus of particles	$\text{Pa}$
$Y^*$	equivalent Young's modulus between two contacting particles	$\text{Pa}$
$z, z^+$	height above the ground and dimensionless height	$\text{m}, 1$
$z_0$	the aerodynamic roughness	$\text{m}$
$z_{salt}$	saltation height	$\text{m}$
$\beta$	damping coefficient of collisional forces	$1$
$\gamma_s=0.5, \gamma_r=0.1$	coefficients of static and rolling friction	$1$
$\zeta_{p,i}$	charge-to-mass ratio of particle $i$	$\text{C kg}^{-1}$
$\eta_n$	residual of EEMD or EMD	-
$\theta, \varphi$	rebouncing angles of particles	$^\circ$
$\kappa \approx 0.41$	von Kármán constant	$1$
$\tau_p$	particle momentum flux	$\text{Pa}$
$\vec{\omega}_{p,i}$	angular velocity of the particle $i$	$\text{rad s}^{-1}$
$\delta_n, \delta_t$	normal and tangential overlap between two contacting particles	$\text{m}$
$\mu=1.8 \times 10^{-5}$	dynamic viscosity of the air	$\text{Pa}\cdot\text{s}$
$\nu=0.3$	Poisson's ratio of particles	$1$
$\xi_i$	EEMD component or IMF of EMD	-
$\rho_a=1.174$	air density	$\text{kg m}^{-3}$
$\rho_p=2650$	particle mass density	$\text{kg m}^{-3}$
$\rho_c$	space charge density	$\text{C m}^{-3}$
$\rho_h^i, \rho_h^j$	density of the electrons trapped in the high energy states on the surface of particle $i$ and $j$	$\text{m}^{-2}$
$\sigma$	surface charge density	$\text{C m}^{-2}$
$\sigma_p$	geometric standard deviation of particle sample in the numerical model	$1$
$\chi_N(t, z)$	the $i$ -th level wavelet detail component	-
$\psi_i(t, z)$	the $N$ -th level wavelet approximation component	-
$\Delta q_{ij}$	net increment of the charge of particle $i$ after colliding with particle $j$	$\text{C}$
$\Delta z$	vertical grid size	$\text{m}$

1

2

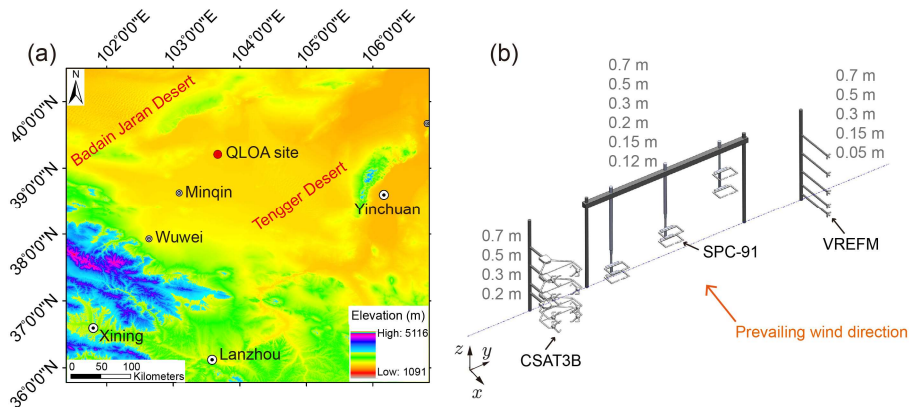
1 **Table 2.** Fitting coefficients of the 3-order polynomial curves in Fig. 5.

Components	$a_{0,i}$	$a_{1,i}$	$a_{2,i}$	$a_{3,i}$	$R^2$
$i = 1$	-2.17	4.02	-2.24	0.31	0.97
$i = 2$	-0.71	2.06	-1.49	0.23	0.80
$i = 3$	0.55	-1.41	1.24	-0.21	0.67

2

3

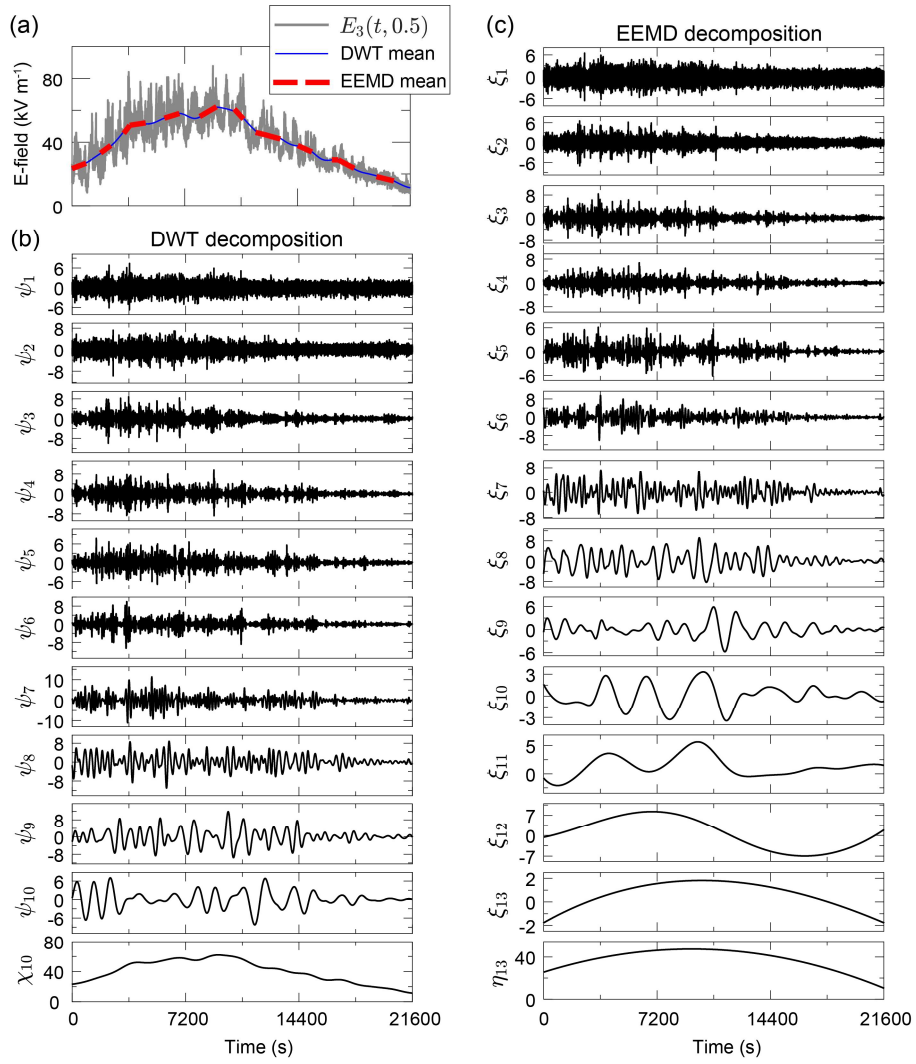
1



2

3 **Figure 1.** Map of the QLOA site and the layout of all instruments. (a) The QLOA site is  
4 located between the Badain Jaran Desert and the Tengger Desert, approximately 90  
5 km northeast of Minqin, Gansu, China. (b) Four CSAT3B sensors were mounted at 0.2-  
6 0.7 m height, respectively; six SPC-91 sensors were mounted at 0.12-0.7 m height,  
7 respectively; total fifteen VREFM sensors were mounted to measure the 3-D E-field at  
8 0.05-0.7 m height, respectively (that is, at each measurement point, three VREFM  
9 sensors are mutually perpendicular). The CSAT3B, SPC-91, and VREFM sensors were  
10 distributed along a straight line parallel to the  $y$  axis, and the prevailing wind  
11 direction in the QLOA site is parallel to the  $x$  axis.

12



2

3 **Figure 2.** The resulting DWT and EEMD components from a measured vertical E-field4 component at 0.5 m height,  $E_3(t, 0.5)$ , with a total of  $N_d=21600$  data points. (a)

5 shows the original E-field time series (gray line), and the time-varying mean obtained

6 by DWT (red line) and EEMD (blue dashed line). (b) shows the detailed components

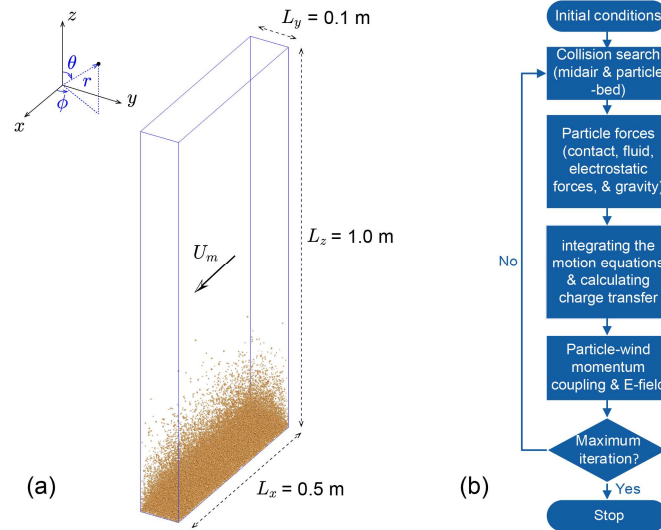
7  $\psi_1 - \psi_{10}$  and approximation component  $\chi_{10}$  of DWT. (c) shows the EEMD8 components  $\xi_1 - \xi_{13}$  and the residue  $\eta_{13}$ . In the EEMD,  $N$  is specified as  $\log_2(N_d) -$ 9 1, the member of ensemble  $N_e$  is 100, and the added white noise in each ensemble

10 member has a standard deviation of 0.2. Times are shown relative to May 6, 2014 at

11 13:00:00 UTC+8.

12

1

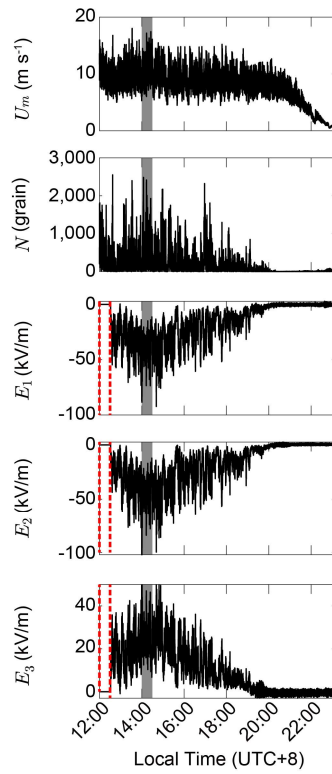


2

3 **Figure 3.** A schematic illustration of the DEM simulation of saltation and the numerical  
4 algorithm of the saltation model. (a) A 3-D view of the simulated wind-blown sand at  
5 the steady state, where the wind shear velocity  $u_* = 0.5 \text{ m s}^{-1}$ , average sand diameter  
6  $d_m = 228 \text{ }\mu\text{m}$ , and geometric standard deviation  $\sigma_p = \exp(0.3)$ . Both the Cartesian and  
7 spherical coordinates are shown in the inset. (b) This flowchart shows the scheme for  
8 simulating the saltation according to the following steps implementing the DEM with  
9 particle triboelectric charging: initial conditions, collision search, particle forces,  
10 integrating motion equations and calculating charge transfer, particle-wind  
11 momentum coupling and evaluating E-field, and finally repeating these execute steps  
12 until reaching the maximum iteration steps.

13

1

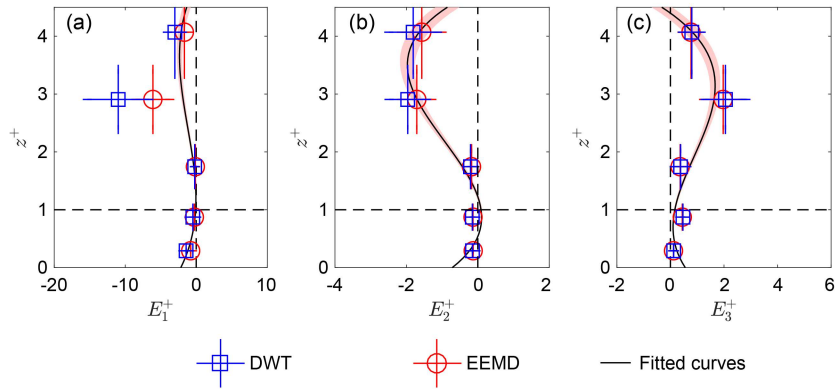


2

3 **Figure 4.** Measured results during a dust storm occurring on May 6, 2014, at the QLOA  
4 site. (a)-(e): the measured time series of the streamwise wind speed,  $u_m$  at 0.7 m;  
5 the number of saltating particle  $N$  at 0.15 m; streamwise E-field  $E_1$ , spanwise E-field  
6  $E_2$ , and vertical E-field  $E_3$  at 0.7 m. Unfortunately, owing to the interruption of power  
7 supply, the 3-D E-field data have not been recorded before  $\sim 12:30$ , as represented by  
8 a dashed box in the last three panels (from top to bottom). The shaded area denotes  
9 the relatively stationary period of the observed dust storm.

10

1



2

3 **Figure 5.** Vertical profiles of the normalized 3-D E-field. Subgraphs (a)-(c), in turn,  
4 correspond to the vertical profiles of  $E_1^+$ ,  $E_2^+$ , and  $E_3^+$  of the observed dust storm.

5 Squares and circles denote the DWT mean and EEMD mean values of the normalized  
6 E-field data, respectively. Error bars are standard deviations. Lines denote robust linear

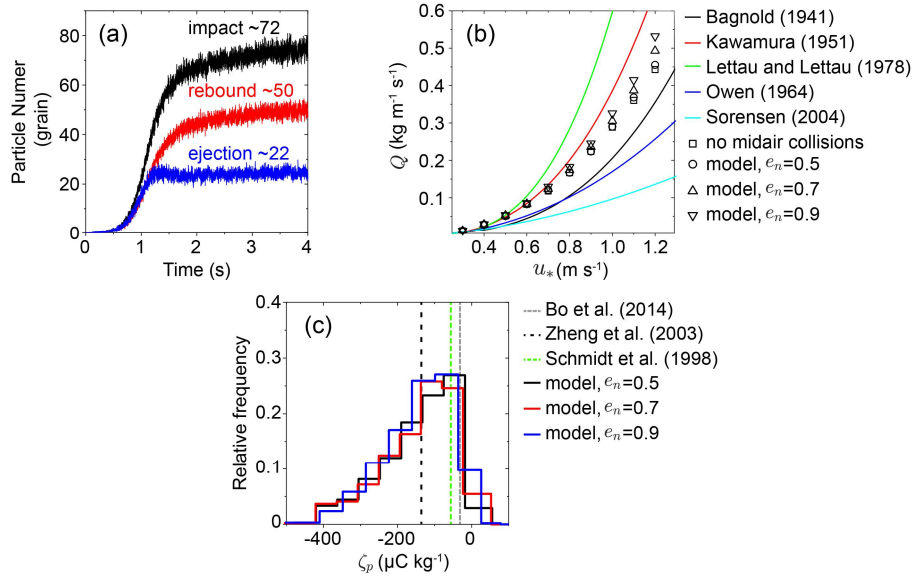
7 least-squares fitting of the normalized E-field data obtained by DWT and EEMD  
8 method using 3-order polynomials (with  $R^2$  of 0.97, 0.80, and 0.67, respectively),

9 where the shaded areas denote 95% confidence bounds.

10



1



2

3 **Figure 6.** Verification of the steady-state numerical model in the case of pure saltation.

4 That is, only vertical E-field needs to be considered, which is produced by the charged

5 saltating particles. (a) The number of the impacting, rebounding, and ejected particles

6 within each time period of  $10^{-4}$  s, where  $u_* = 0.5 \text{ m s}^{-1}$ ,  $d_m = 228 \mu\text{m}$ , and  $\sigma_p = \exp(0.3)$ .

7 (b) Comparison of the simulated total mass flux with the most commonly-used

8 semiempirical saltation mass flux equations (Bagnold, 1941; Kawamura, 1951; Lettau

9 and Lettau, 1978; Owen, 1964; Sørensen, 2004), where  $d_m = 228 \mu\text{m}$ , and  $\sigma_p = \exp$

10 (0.3). (c) Comparison of the simulated charge-to-mass ratio distribution in the range

11 of 0.07-0.09 m height with the measured mean charge-to-mass ratio, in the range of

12 0.06-0.1 m height (Zheng et al., 2003), at 0.05 m height (Schmidt et al., 1998) and 0.08

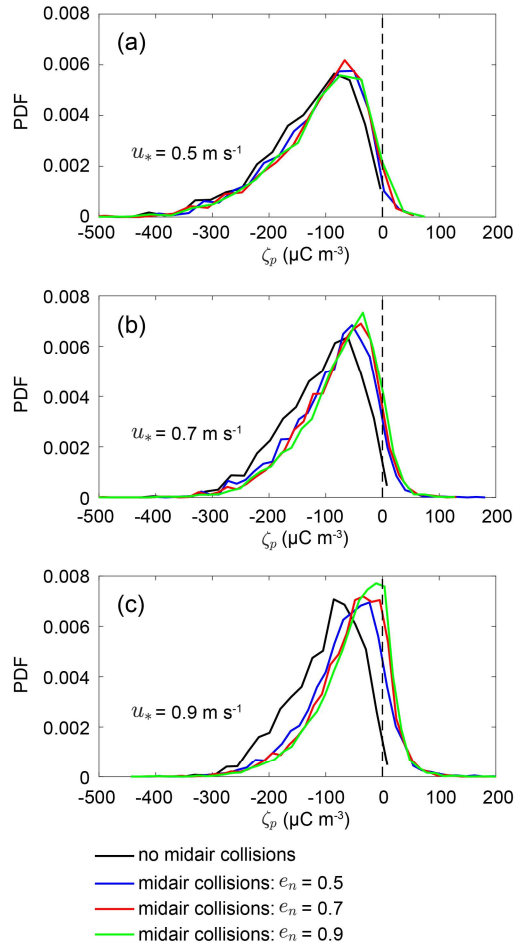
13 m height (Bo et al., 2014). Here,  $\rho_h^0 = 6 \times 10^{15} \text{ m}^{-2}$  is determined by calibrating the model

14 with measurements;  $u_* = 0.35 \text{ m s}^{-1}$ ,  $d_m = 203 \mu\text{m}$ , and  $\sigma_p = \exp(0.33)$  are estimated

15 from (Zheng et al., 2003).

16

1

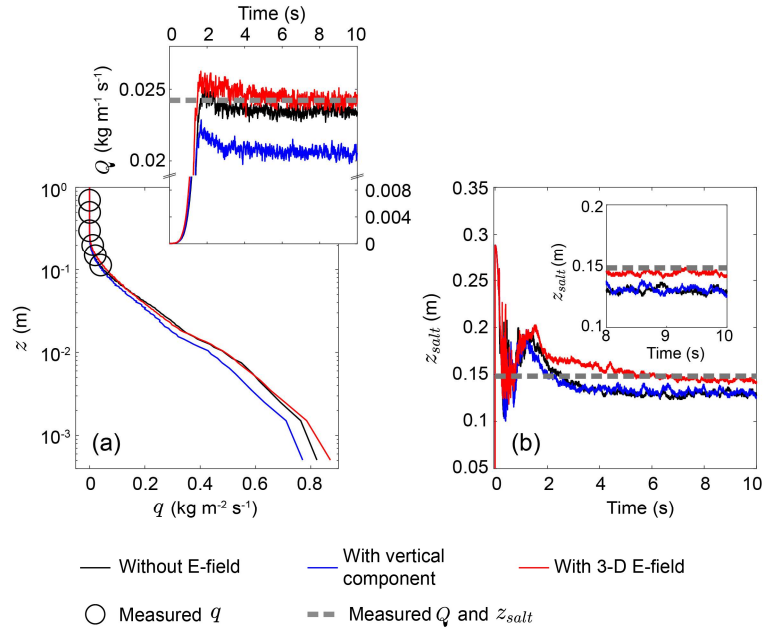


2

3 **Figure 7.** Effects of midair collisions on the probability density function (PDF) of charge-  
4 to-mass ratio of saltating particles for various wind velocities (a)  $u_* = 0.5 \text{ m s}^{-1}$ , (b)  
5  $u_* = 0.7 \text{ m s}^{-1}$ , and (c)  $u_* = 0.9 \text{ m s}^{-1}$ , where  $d_m = 203 \mu\text{m}$ ,  $\sigma_p = \exp(0.33)$ , and  $\rho_h^0 = 6 \times 10^{15}$   
6  $\text{m}^{-2}$ .

7

1

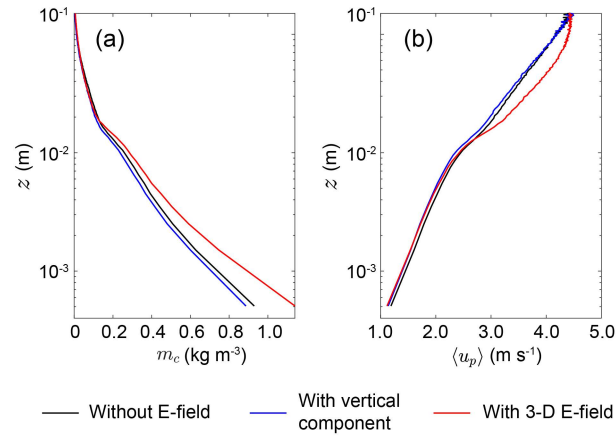


2

3 **Figure 8.** Comparison of the simulated mass flux  $q$  and total mass flux  $Q$  (a) and  
 4 saltation height  $z_{salt}$  (b) with our measurements in the relatively steady period of the  
 5 observed dust storm (shaded in Fig. 4 and Fig. S3 in the Supplement), where  $u_* = 0.37$   
 6 m s<sup>-1</sup>,  $d_m = 200 \mu\text{m}$ ,  $\sigma_p = \exp(0.42)$ ,  $\rho_h^0 = 6 \times 10^{15} \text{ m}^{-2}$ , and  $e_n = 0.7$ . (a) Circles are the  
 7 measured mean mass flux, dashed line denotes the estimated mean total mass flux,  
 8 and lines denote the simulated results. (b) Dashed lines denote the estimated saltation  
 9 height based on our measurements and lines denote simulated results. The  
 10 uncertainty analysis of the measured or estimated results can be found in Text S1 in  
 11 the Supplement.

12

1



2

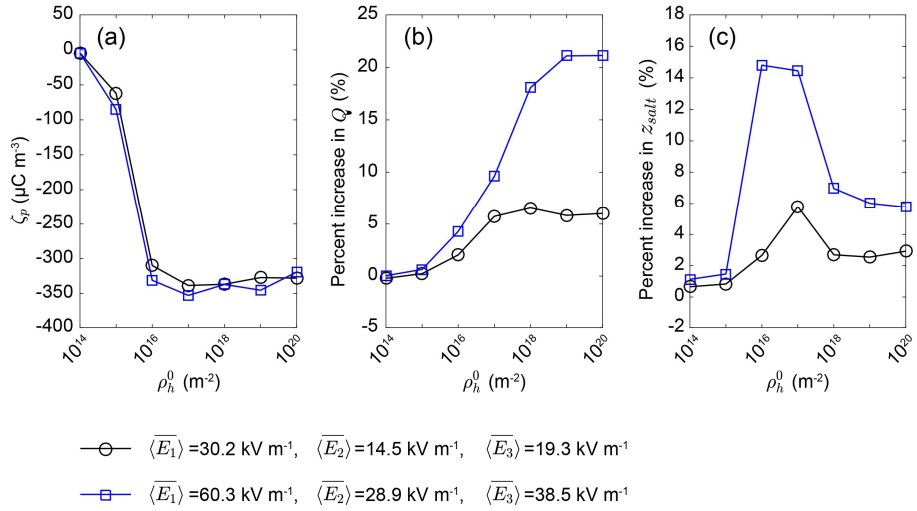
3 **Figure 9.** Vertical profiles of the particle mass concentration  $m_c$  and mean particle

4 horizontal speed  $\langle u_p \rangle$  for different cases, where  $u_* = 0.37 \text{ m s}^{-1}$ ,  $d_m = 200 \text{ }\mu\text{m}$ ,

5  $\sigma_p = \exp(0.42)$ ,  $\rho_h^0 = 6 \times 10^{15} \text{ m}^{-2}$ , and  $e_n = 0.7$ .

6

1



2

3 **Figure 10.** Effects of the density of charged species  $\rho_h^0$  on saltation for two different  
4 height-averaged time-varying mean levels (i.e.  $\langle \bar{E}_i \rangle$ ,  $i = 1,2,3$ ). (a) The mean charge-  
5 to-mass ratio  $\zeta_p$  (in the range from 0.07 to 0.09 m height) as a function of  $\rho_h^0$  ranging  
6 from  $10^{14}$  to  $10^{20} \text{ m}^{-2}$  (e.g. Kok and Lacks, 2009). (b) Percent increase in the total mass  
7 flux  $Q$  as a function of  $\rho_h^0$ . (c) Percent increase in the saltation height  $z_{salt}$  as a  
8 function of  $\rho_h^0$ . The squares correspond to the height-averaged time-varying mean in  
9 the steady stage of the observed dust storm (shaded in Fig. S7 in the Supplement). In  
10 these cases,  $e_n=0.7$ .